Nuclear Engineering and Technology 55 (2023) 2854–2863

Contents lists available at ScienceDirect

Nuclear Engineering and Technology

journal homepage: www.elsevier.com/locate/net

Original Article

Hybrid model-based and deep learning-based metal artifact reduction method in dental cone-beam computed tomography☆

Jin Hur [a], Yeong-Gil Shin [a], Ho Lee [b, *]

[a] Department of Computer Science and Engineering, Seoul National University, 1 Gwanak-ro, Gwanak-gu, Seoul, 08826, Republic of Korea
[b] Department of Radiation Oncology, Yonsei Cancer Center, Heavy Ion Therapy Research Institute, Yonsei University College of Medicine, 50-1 Yonsei-ro, Seodaemun-gu, Seoul, 03722, Republic of Korea

ARTICLE INFO

Article history:
Received 8 March 2023
Received in revised form
23 April 2023
Accepted 12 May 2023
Available online 19 June 2023

Keywords:
CBCT
Metal artifact reduction
Beam-hardening correction
Reconstruction
Polychromatic X-ray attenuation coefficient
Deep learning

ABSTRACT

Objective: To present a hybrid approach that incorporates a constrained beam-hardening estimator (CBHE) and deep learning (DL)-based post-refinement for metal artifact reduction in dental cone-beam computed tomography (CBCT).
Methods: Constrained beam-hardening estimator (CBHE) is derived from a polychromatic X-ray attenuation model with respect to X-ray transmission length, which calculates associated parameters numerically. Deep-learning-based post-refinement with an artifact disentanglement network (ADN) is performed to mitigate the remaining dark shading regions around a metal. Artifact disentanglement network (ADN) supports an unsupervised learning approach, in which no paired CBCT images are required. The network consists of an encoder that separates artifacts and content and a decoder for the content. Additionally, ADN with data normalization replaces metal regions with values from bone or soft tissue regions. Finally, the metal regions obtained from the CBHE are blended into reconstructed images. The proposed approach is systematically assessed using a dental phantom with two types of metal objects for qualitative and quantitative comparisons.
Results: The proposed hybrid scheme provides improved image quality in areas surrounding the metal while preserving native structures.
Conclusion: This study may significantly improve the detection of areas of interest in many dentomaxillofacial applications.

1. Introduction

Dental cone-beam computed tomography (CBCT) is a well-known imaging modality for implant site imaging, maxillofacial diagnosis, orthodontics, and treatment planning in craniofacial surgery. Despite being a secure and reliable diagnostic method, CBCT suffers from high-density objects such as metal implants and dental fillings. Such metal objects cause strong beam hardening effects that significantly alter the energy spectrum of a beam, resulting in prominent streak-like artifacts and shadows in CBCT images that reduce the contrast, obscure the structure, and impair the detection of areas of interest. Therefore, the degradation of CBCT image quality makes diagnosis challenging and time-consuming.

Metal artifact reduction (MAR) techniques for CBCT have been widely studied [1–15]. One approach involves mathematical correction-based algorithms, which enhance the reconstructed image by reducing beam-hardening artifacts and correcting the error model. Hsieh et al. proposed a polynomial error model with certain assumptions [16]. The error model was approximated with a relatively simple form, reducing the computational complexity of the estimation process. They demonstrated that two iterations are generally sufficient to deal with a wide range of densities. Park et al. proposed a beam-hardening corrector that accurately reflected the characteristics of beam hardening [17]. They demonstrated the corrector's performance using numerical simulations and phantom experiments. However, in the presence of several high-density metals, the metal regions in the sinogram are severely corrupted,

☆ Please cite this article as: Jin Hur et al. Hybrid Model- and Deep Learning-Based Metal Artifact Reduction Method in Dental Cone-Beam Computed Tomography, Nuclear Engineering and Technology (2023), https://doi.org/10.1016/j.net.2023.00.000.

* Corresponding author.
E-mail addresses: redquire@snu.ac.kr (J. Hur), yshin@snu.ac.kr (Y.-G. Shin), holee@yuhs.ac (H. Lee).

https://doi.org/10.1016/j.net.2023.05.016

and the performance of this method is limited. Shi et al. analyzed the variation in the attenuation coefficient of several materials at an energy level and discovered that these attenuation coefficients exhibit a similar shape of variation with only a scale difference [18]. From this perspective, they proposed a synthetic geometry projection that combined each material in the projection with a scaled material. Hur et al. proposed a constrained beam-hardening estimator (CBHE), leading to faster computation without compromising MAR quality [19]. These estimator-associated parameters were calculated numerically from an uncorrected CT image and metal-only forward projection.

Another approach involves deep learning (DL)-based techniques such as U-net [20] and convolutional neural networks (CNNs) [21], which can refine the results of interpolation-based algorithms or directly correct metal artifacts by training with supervised learning. However, supervised learning requires anatomically identical CT image pairs, with and without metal artifacts, which are clinically impractical to obtain. Adversarial training has recently been studied as a novel method for image-to-image translation [22]. Isola et al. suggested a conditional generative adversarial network (CGAN), which is composed of two networks: a generator network for performing image-to-image translation and a discriminator network for the disentanglement of artifacts from CT [23,24]. Because training networks with a mean-square error loss function have shown over-smoothed images [25], they presented a traditional loss coupled with an adversarial loss working excellent overall for image-to-image translation tasks. Liao et al. proposed a CycleGAN-based artifact disentanglement network that separates metal artifacts and normal tissues from CT images in latent space [26]. It was the first unsupervised method for CT and showed quantitative evaluation results against other supervised/unsupervised MAR methods with synthesized data. While preserving the native anatomical structures of the patients, image correction should focus on corrupted regions and recover hidden features caused by metal artifacts. GAN-based methods tend to degrade unaffected regions by metal artifacts as the training data barely cover various artifact patterns. Several researchers have investigated the use of two enhancement networks for dual domain image processing, specifically for sinogram and CT image restoration [27,28]. These networks are built on general image enhancement technique. The joint utilization of two domains have shown superior performance compared to other studies. Wang et al. proposed a dual domain network framework that effectively incorporates the constraints of the intrinsic imaging geometry model into the process of mutual learning between spatial (CT) and Radon (sinogram) domains [29]. Additionally, this framework can be flexibly integrated with prior learning from both domains. Notably, this approach is distinguished by its specificity in aligning neural network modules and algorithm operations, which establishes a clear working mechanism.

In a previous study, we implemented CBHE derived from a polychromatic X-ray attenuation model with respect to the X-ray transmission length, which calculates associated parameters numerically. In this study, we established that DL-based post-refinement with the artifact disentanglement network (ADN) [26] can be improved significantly without incurring excessive computational costs when this CBHE remains in dark-shaded regions around the metal. This network is trained to learn the unsupervised mapping between metal artifact-corrupted CT images and their corresponding metal artifact-free images. The network uses the CycleGAN architecture, which consists of two generators and two discriminators to learn the mapping between two domains: the generators are used to translate the CBCT images with metal artifacts to the artifact-free domain, whereas the discriminators are used to distinguish between the translated and real artifact-free images. The reconstructed images generated by the CBHE are normalized to include the content from the air to the bone region unaffected by artifacts. Performing ADN with data normalization replaces metal regions with values from the bone or soft tissue regions. Finally, the metal regions obtained from the CBHE are blended into the reconstructed images.

2. Material and methods

2.1. Metal segmentation and X-ray transmission length calculation

Because the CBHE uses information on the transmission length of X-rays through the metal region, a segmented metal region in the CBCT image is required. A threshold-based technique is generally used for the metal segmentation of CBCT images. Metal artifacts appear as white streaks or dark shadows that extend radially around the metal region. Generally, a few points separate these artifacts from the metal region values, and the metal region can be separated by specifying a threshold. Because, in a few cases, distinguishing between artifacts and metal regions is challenging, so adaptive filtering or mean-shift techniques can also be applied to weaken the streaks.

The X-ray transmission length for the metal region in each projection was calculated using the segmented metal region. The segmented metal region was converted into a binary mask, and CT scan geometry for each projection was required. The process of calculating the X-ray transmission length for each pixel on the projection is very similar to the pixel-driven ray casting of the volume-rendering process. The intersection lengths between each line r from the position of the X-ray source to the pixels on the projection P and each voxel of the metal region in the CT volume are determined and accumulated. Because the CT value in the voxel of the metal region is not considered, the entire process can be transformed into line integrals for the binary mask of the metal region as

$$l_r = \sum_{i=1}^{n} l_i = \int_r M ds, \tag{1}$$

where M is a binary mask consisting of one for metal voxels and zero for nonmetal voxels (see Fig. 1).

2.2. Metal artifact reduction method with constrained beam-hardening estimator

Photons emitted from an X-ray tube do not have the same energy. The attenuation in the projections is underestimated when polychromatic X-ray photons penetrate an irradiated object as they shift to higher energies. The underestimated error in projections is the accumulation of reduced polychromatic X-ray attenuation coefficients along the transmission length. The beam-hardening error (BHE) $\psi_s(l)$ can be represented by the polychromatic X-ray attenuation coefficient $\widehat{\mu_s}(l)$ for the material s, transmission length l, and the normalized X-ray spectrum $\eta(E)$ with $E \in [E_m, E_M]$ as

$$\psi_s(l) = \widehat{\mu_s}(0)l + ln\left(\int_{E_m}^{E_M} \eta(E) * exp\{-\mu_s(E)l\} dE\right). \tag{2}$$

Here, $ln(\int_{E_m}^{E_M} \eta(E) * exp\{-\mu_s(E)l\} dE)$ depends on the X-ray spectrum $\eta(E)$ and material attenuation coefficient $\mu_s(E)$. By applying the constrained approximations in Ref. [19], Eq. (2) can be

approximated using the CBHE $\tilde{\psi}_s(l)$ as

$$\psi_s(l) \approx \tilde{\psi}_s(l) = \widehat{\mu_s}(0)l - \mu_s(E_M)l + \alpha^* ln\left(\frac{1 - exp\{\widehat{\mu_s}(0)l\}}{\widehat{\mu_s}(0)l}\right). \quad (3)$$

Dependencies can be avoided by constrained approximation, leading to a faster computation. Finally, the BHE can be derived in the following linear form as

$$\tilde{\psi}_s(l) = \beta\tilde{\psi}_{s,1}(l) + \alpha\tilde{\psi}_{s,2}(l), \quad (4)$$

where

$$\beta = \widehat{\mu_s}(0) - \mu_s(E_M),$$

$$\tilde{\psi}_{s,1}(l) = l,$$

$$\tilde{\psi}_{s,2}(l) = ln\left(\frac{1 - exp\{-\mu_s(E_H)l\}}{\mu_s(E_H)l}\right). \quad (5)$$

Fig. 2 shows a comparison between the CBHE and BHE in titanium, iron, and copper. The CBHE was calculated by excluding $\tilde{\psi}_1(l)$. For each metal, the model-associated unknown parameter was determined to have the shape closest to the given BHE curve. For up to 50 mm, the CBHE showed a proximity with the BHE.

The corrected projection can be expressed as $P + \tilde{\psi}_s(l)$. Because the FDK operation [30] has linearity, the corrected CT image can be expressed as

$$R^{-1}(P + \tilde{\psi}_s(l)) = R^{-1}(P) + R^{-1}(\tilde{\psi}_s(l)) = f_{CT} + \beta R^{-1}(\tilde{\psi}_{s,1}(l)) + \alpha R^{-1}(\tilde{\psi}_{s,2}(l)), \quad (6)$$

where R^{-1} indicates the FDK operator and $R^{-1}(P)$ is the uncorrected CT f_{CT}.

Constrained beam-hardening estimator has only been considered for a single metallic object thus far. However, in many cases, different metals are present in the scanned area. By analyzing the variation of the attenuation coefficients of the materials based on the energy level, the attenuation coefficients showed a similar shape of change with only different scales. Therefore, considering

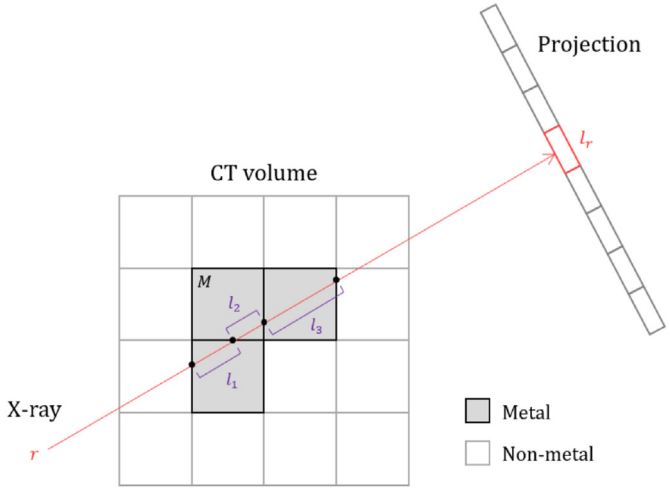

Fig. 1. Calculation of X-ray transmission length.

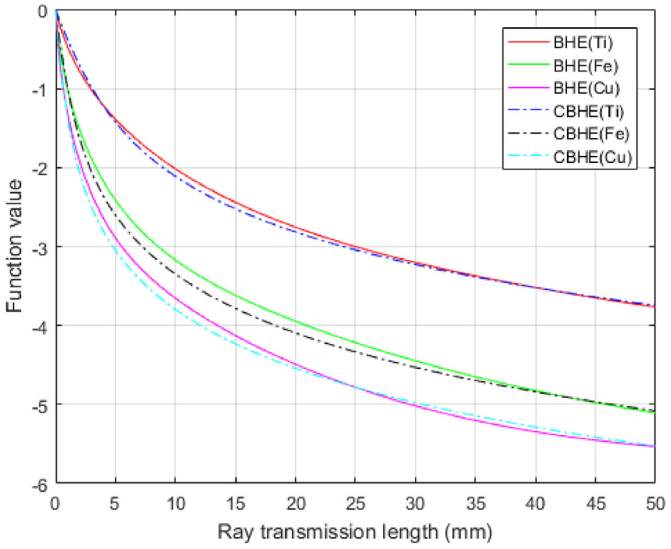

Fig. 2. Correspondence between the BHE and the CBHE when the ray transmission length is < 50 mm for titanium (Ti), iron (Fe), and copper (Cu).

that a few of the artifacts caused by the high-density metal can be replaced with those caused by the low-density metal, the MAR algorithm requires slight modification in the metal segmentation.

First, the MAR method is performed sequentially from the lowest-density metal to the highest-density metal in the entire metal area. For each step of metal segmentation, the metal area contains not only the area of the current metal but also the area of the higher-density metals (Fig. 2). Therefore, the CBHE can mitigate artifacts not only between the same metals but also between different metals. Equation (6) can be modified as

$$R^{-1}\left(P + \sum_{k=1}^{n}\tilde{\psi}_{s_k}(l)\right) = R^{-1}(P) + R^{-1}\left(\sum_{k=1}^{n}\tilde{\psi}_{s_k}(l)\right)$$

$$= f_{CT} + \sum_{k=1}^{n}\beta_k R^{-1}(\tilde{\psi}_{s,1}(l)) + \sum_{k=1}^{n}\alpha_k R^{-1}(\tilde{\psi}_{s,2}(l)). \quad (7)$$

The reconstructions of $R^{-1}(\tilde{\psi}_1(l))$ and $R^{-1}(\tilde{\psi}_2(l))$ are performed once during the entire process. They are used to alleviate the beam-hardening effect on f_{CT} following Eq. (5). $\widehat{\mu_s}(0)$ should be calculated. However, obtaining additional information is challenging about the material attenuation properties (e.g., X-ray mass attenuation coefficient table [31]). Thus, if the obtaining task is not possible, empirically, the lowest value of the metal region in the CT image before HU conversion is close to $\widehat{\mu_s}(0)$. Therefore, the lowest value can be an alternative. β compensates for the entire metal region only with the same value, and its value is irrelevant as long as β makes $R^{-1}(\tilde{\psi}_1(l))$ larger than the maximum amount reduced by $R^{-1}(\tilde{\psi}_2(l))$. α is an unknown coefficient that minimizes the beam-hardening error. This condition can be obtained by solving the problem of minimizing the following function.

$$\underset{\alpha}{\operatorname{argmin}}\left(SD\left(f_{CT}(x) + \alpha R^{-1}(\tilde{\psi}_{s,2}(l))(x)\right)\right) \quad for\ M(x) > 0, \quad (8)$$

where SD indicates the standard deviation operator and $M(x)$ is the mask image representing the metal region. The detailed algorithm is presented in Algorithm 1, and Fig. 3 shows the entire process of the CBHE method.

Algorithm 1. MAR with CBHE for multiple types of metal

Algorithm 1. MAR with CBHE for multiple types of metal

1: Reconstruct a CT image *f* using FDK.
2: Segment the entire metal region M from *f*.
3 Identify the types of the contained metals S = (s_1, s_2, …., s_n) and the area $M_i \in M$
4 Select the metal s_k of the lowest density in S.
5: Generate $\tilde{\psi}_1(l)$ projections by computing the ray transmission length along M through forward projection.
6: Generate $\tilde{\psi}_2(l)$ projections by (5) using the ray transmission length.
7: Reconstruct $R^{-1}\left(\tilde{\psi}_{s_k,1}(l)\right)$ and $R^{-1}\left(\tilde{\psi}_{s_k,2}(l)\right)$ using FDK.
8 Find out the unknown coefficient α_{s_k} by minimizing the energy function defined as (8).
9: Remove s_k from S and M_k from M.
10: If S is not empty, then go to 4
11: Generate the final CT image by (7).

2.3. Post-refinement with DL-based network model

Although the CBHE-based MAR method may recover information corrupted by beam-hardening artifacts, it is not appropriate for artifacts caused by factors other than beam hardening. Therefore, a few artifacts can remain in the MAR results. Image-domain MAR methods focus on identifying and removing artifacts from the CT images. In research on image processing techniques as a post-processing strategy, MAR methods based on DL have recently been studied. Studies based on GAN [22] are quite effective [32].

Among the GAN-based MAR methods, the CycleGAN-based artifact disentanglement network (ADN) [26] can be used to separate metal artifacts and normal tissues from CT images in the latent space. This approach involves training a deep neural network to learn the mapping between input and target image spaces, where the input space includes the original CT image and the target space includes the CT image with the metal artifact removed (see Fig. 4). The network architecture generally consists of a generator and discriminator. The generator transforms the input CT image into a target image that does not contain metal artifacts. The discriminator was used to distinguish between the transformed and real target images. This is repeated cyclically with the

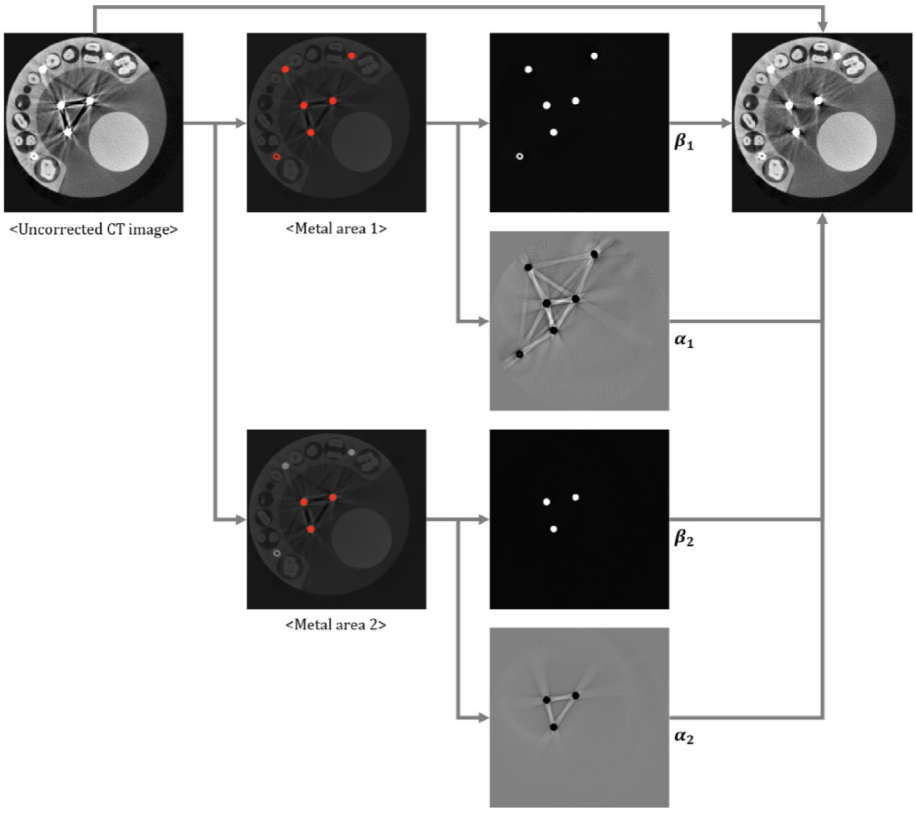

Fig. 3. Illustration of the entire process of CBHE when containing two types of metal objects.

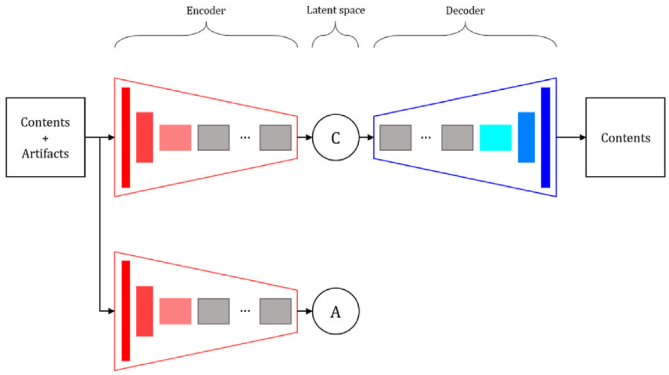

Fig. 4. MAR process of ADN network.

generator trying to produce increasingly accurate transformed images, whereas the discriminator becomes better at distinguishing between real and generated target images. The key innovation of this approach is the use of latent space to separate metal artifacts from normal tissues in CT images. This is achieved by training the generator to transform the input image into the target image while minimizing the distance between the input and generated images in the latent space. This enables the network to disentangle metal artifacts from normal tissues in the input image, resulting in a target image that reflects the underlying anatomy accurately.

The CBHE-based mathematical correction method and ADN have features that complement each other's shortcomings. The CBHE method reduces the artifact complexity of CBCT images rapidly, and the remaining artifacts can be reduced through the ADN effectively. The author of ADN provided pretrained models that were trained using DeepLesion [33] and Spineweb [34] datasets, respectively. We attempted to train a new model by combining both datasets. For the Adam optimizer, we set the initial learning rate to 0.001 and used (0.5, 0.999) for beta. The hyper-parameters for each loss term were consistent with those stated by the author, which were 1.0 for adversarial losses and 20.0 for reconstruction, artifact consistency, and self-reduction losses. Metal regions were defined as regions with HU values greater than 2500. However, the new model combining the two datasets did not show significant differnce in performance compated to the pretrained models. In the end, we used the pretrained model using Spineweb. To apply ADN, we implemented additional modules that deal with the input and output of both CBHE and ADN methods. These modules include normalization/denormalization component and a complement that supplements metal regions removed by ADN.

The overall process is illustrated in Fig. 5. As the ADN network takes a normalized image in the range of [−1, 1] as input, data normalization is performed to load the MAR results from the CBHE method. A normalization range should contain unaffected regions from the air to the bones. After preparation, an artifact-free image was generated using the ADN. The metal region in the artifact-free image was replaced by values in the bone or soft-tissue regions. Therefore, the metal regions obtained in the previous CBHE process should be blended. Furthermore, because ADN supports 256 × 256 input images only, downsampling before normalization and upsampling after denormalization are required.

2.4. Experimental evaluation

A dental phantom with two metal types (JawEquivPhantom) is used to evaluate the performance of the conventional sinogram-inpainting methods (LIMAR and NMAR), recent model-based method (CBHE), and post-refinement of ADN to each MAR

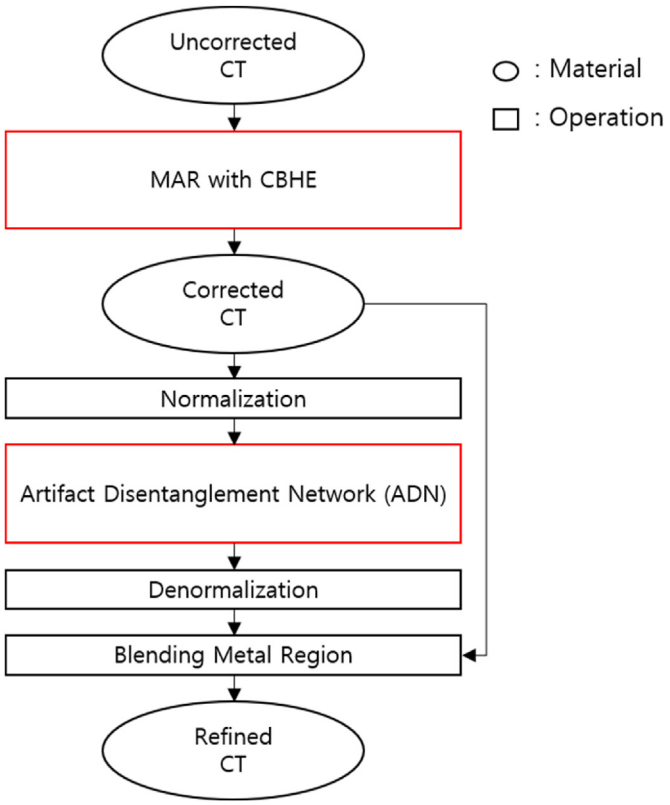

Fig. 5. Process of the collaboration with ADN.

method, as shown in Fig. 6. With a similar structure to the mandibular, JawEquivPhantom consists of bones, teeth, and aluminum and titanium rods. It was scanned using a cone-beam CT (CBCT) system (Ray Co., Korea) with a peak voltage of 90 keV. The source-to-axis is 468 mm and the source-to-detector is 661 mm. The projection has a resolution of 786 (w) × 960 (h) pixels with a detector pitch size of 0.15 mm. The reconstructed image has a resolution of 512 × 512 × 256 voxels and a voxel pitch size of 0.18 mm. Water correction was not applied to the dental phantom before performing MAR methods.

For quantitative evaluation, two metrics were employed: mean absolute deviation (MAD) [9] and contrast-to-noise ratio (CNR) [35]. Because of the lack of reference images, the MAD was computed on the outside part of the metal area in regions of interest (ROIs) by referencing the homogeneous region of the uncorrected image. The CNR was computed for the two selected regions, i.e., bone and air areas.

$$MAD(HU) = \frac{1}{N} * \sum_{i \in ROI} \left| x_i^{MAR} - x_i^{True} \right|, \tag{9}$$

$$CNR = \frac{2|M_A - M_B|}{\sqrt{\sigma_A^2 + \sigma_B^2}}, \tag{10}$$

where x_i^{MAR} and x_i^{True} denote the ith HU value of the ROI in the corrected and reference images, respectively, and N is the total number of selected ROIs. M_A and M_B denote the mean value of each region A and B in the CBCT, respectively, and σ_A and σ_B are the standard deviations.

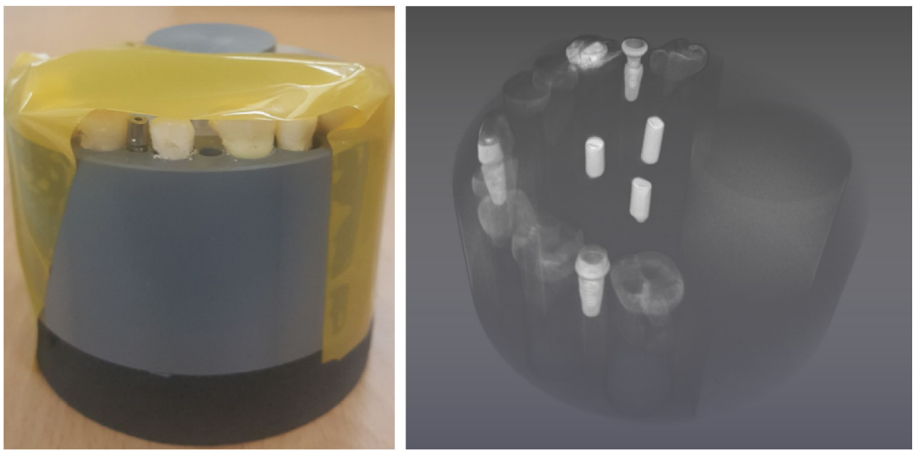

Fig. 6. Photo and 3D visualization (emphasized metal region with transparent overall volume) of JawEquivPhantom.

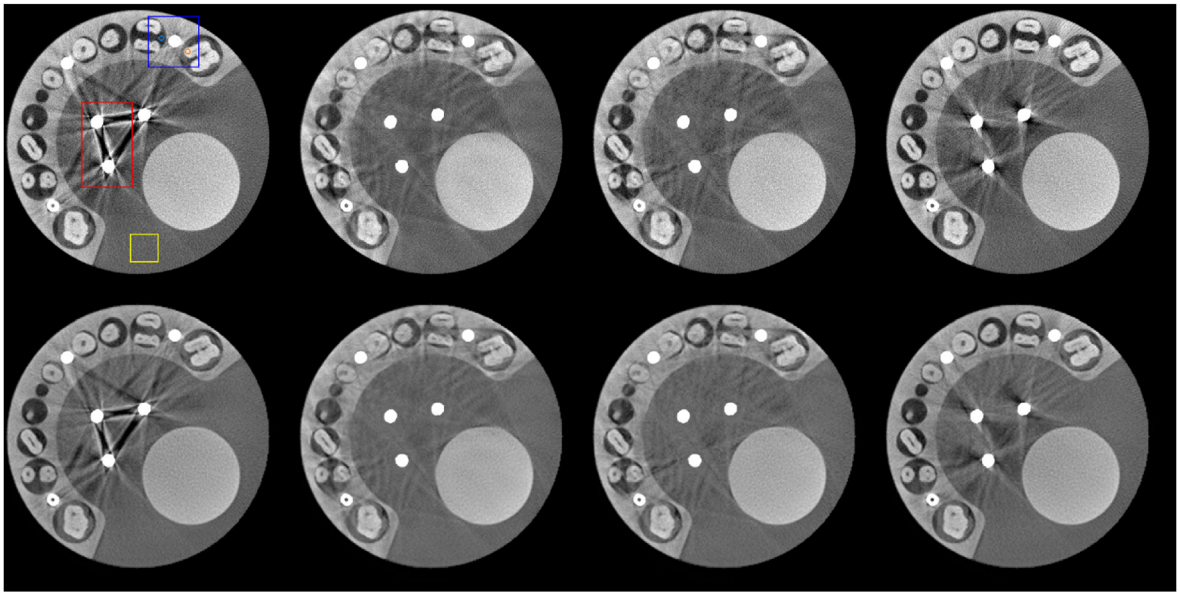

Fig. 7. Comparison of conventional and hybrid MAR methods for JawEquivPhantom. From the left, the uncorrected image, LIMAR result, NMAR result, and CBHE result are shown. The first row shows the results of each method and the second row shows adding ADN to each MAR method. The reconstruction images are displayed at window (center and width) settings of (500, 3000) HU.

3. Results

Fig. 7 shows a comparison among the three MAR methods: LIMAR, NMAR, and CBHE, for the JawEquivPhantom. The top row shows the reconstructed CBCT images generated using each method on the uncorrected CBCT images. The bottom row shows the application of post-refinement using ADN on the initial metal artifact-reduced image obtained by each method. All methods reduced the beam-hardening artifacts shown in the uncorrected CBCT images. Furthermore, LIMAR and NMAR with ADN significantly suppressed dark and white streak artifacts. However, it lost morphological information around the metal region and introduced secondary artifacts (Fig. 9).

Table 1 lists the quantitative results of each method. Additionally, MAD was calculated on ROI1 in Fig. 8 (red box in Fig. 7) by referring to the homogeneous ROI (yellow box in Fig. 7). The CNR was calculated using the orange and blue circles in Fig. 9 (blue box in Fig. 7).

Comparing ADN to each MAR method, only relatively small amounts of artifacts without morphological loss were reduced. Cooperation between ADN and each MAR method showed significantly improved results. The remaining dark shadows and a few

Table 1
Quantitative evaluation of the MAR methods for ROIs of JawEquivPhantom.

Methods	Uncorrected	Uncorrected + ADN	LIMAR	LIMAR + ADN	NMAR	NMAR + ADN	CBHE	CBHE + ADN
MAD	458.15	312.80	118.13	68.16	132.08	79.50	318.35	194.14
CNR	13.32	14.06	7.22	6.73	5.45	5.53	14.20	17.17

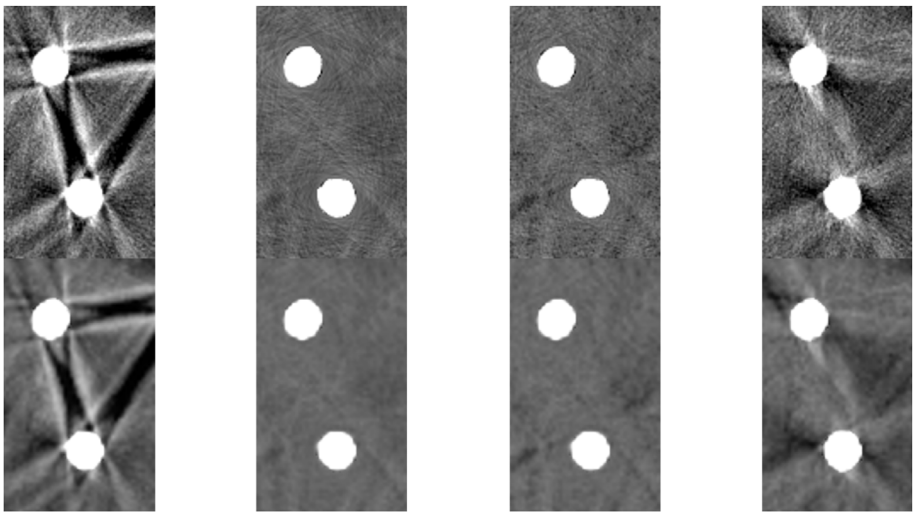

Fig. 8. Zoomed CBCT images for ROI1 (the red box) in Fig. 7. From the left, the uncorrected image, LIMAR result, NMAR result, and CBHE result are shown. The first row shows the results of each method and the second row shows adding ADN to each MAR method. These images are displayed at window (center and width) settings of (500, 3000) HU.

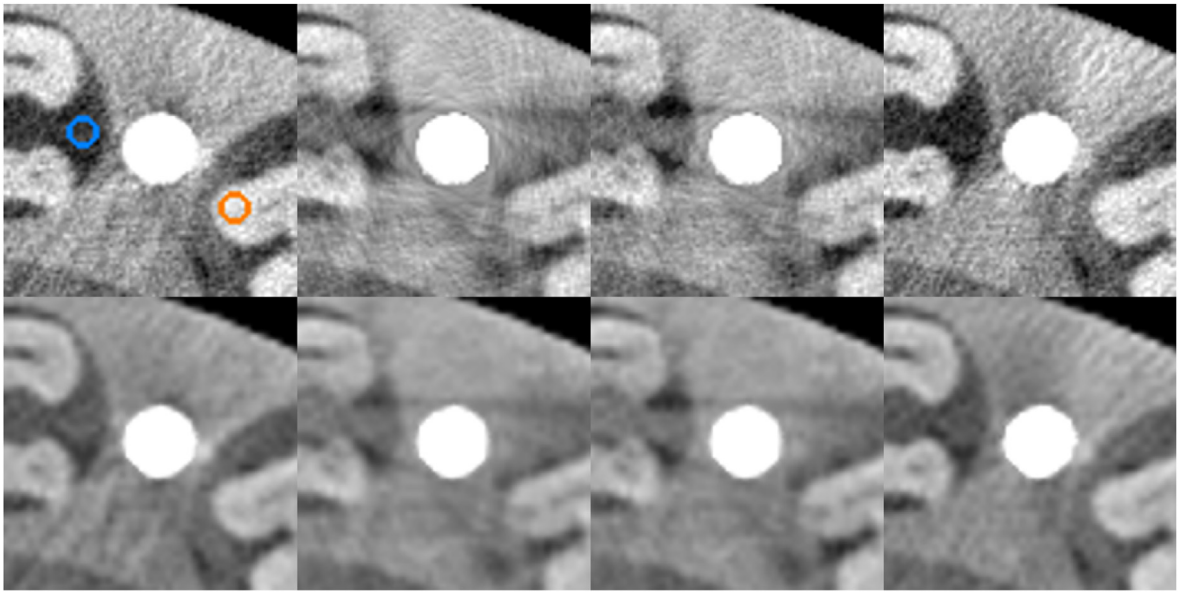

Fig. 9. Zoomed CBCT images for ROI2 (the blue box) in Fig. 7. From the left, the uncorrected image, LIMAR result, NMAR result, and CBHE result are shown. The first row shows the results of each method and the second row shows adding ADN to each MAR method. These images are displayed at window (center and width) settings of (500, 3000) HU. (For interpretation of the references to colour in this figure legend, the reader is referred to the Web version of this article.)

white streaks around the metal region in the center were reduced significantly in cooperation with ADN and CBHE. The result of the collaboration shows a 39% improvement over the CBHE method and a 38% improvement over the ADN method in terms of MAD (Table 1). In terms of CNR, it demonstrated a 21% improvement compared with the CBHE-based MAR method and 22% improvement compared with the ADN method. Although the others showed better results in terms of MAD, they showed little better (NMAR) or poorer results (LIMAR) in CNR.

Fig. 10 demonstrates that residual artifacts can be effectively removed when CBHE is first applied to the bone and then ADN is used. It can be observed that the performance of reducing residual artifacts is better in the order of 1) using ADN after applying CBHE to metal and bone, 2) applying CBHE to metal and bone, 3) using ADN after applying CBHE to metal only, and 4) applying CBHE to metal only.

4. Discussion

The proposed hybrid MAR approach based on CBHE and ADN is in sharp contrast to previous MAR approaches, and it can improve clinical diagnosis and treatment planning in a wide range of clinical applications. Furthermore, CBHE-based mathematical correction is a model-based approach that considers the physics of the CT imaging process and uses the energy-dependent attenuation coefficients of the materials in the CT image to estimate the photon

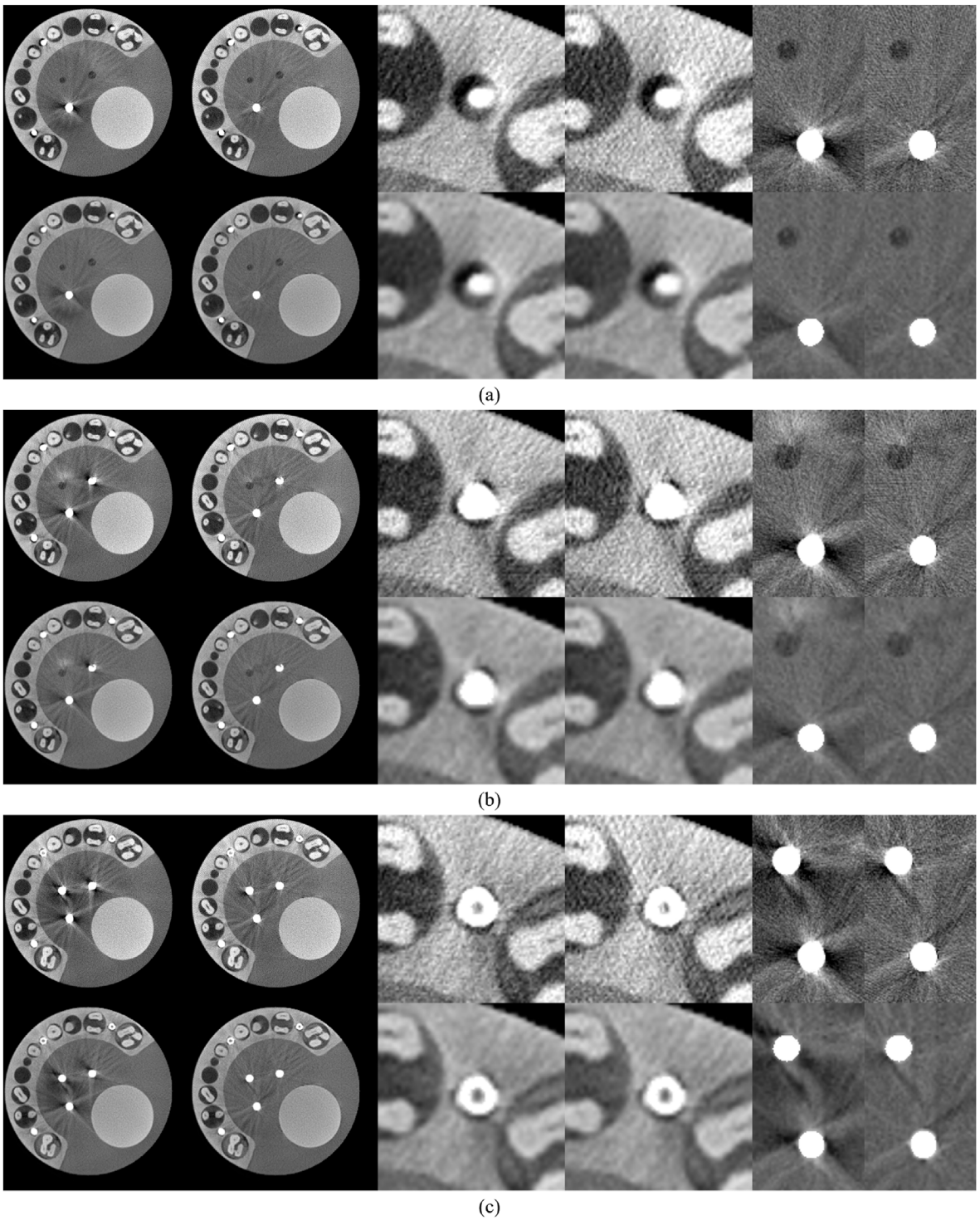

Fig. 10. Comparison of CBCT images generated by applying CBHE based on metal only and CBHE based on metal and bone for JawEquivPhantom, with the representative slices with metal counts of one (a), two (b), and three (c) in the center. From left to right, the odd columns show the results of applying CBHE based on metal only and the even columns show the results of applying CBHE based on metal and bone. The first row is the result before using ADN and the second row is the result after using ADN for each result. The reconstruction images are displayed at window (center and width) settings of (500, 3000) HU.

flux that passes through the metal object and the corresponding beam hardening effect. An ADN-based post-refinement step is a data-driven approach that uses deep neural networks to learn the mapping between metal artifact-corrupted CT images and their corresponding artifact-free images. By combining these two approaches, the hybrid method can exploit the strengths of model-based and data-driven approaches, leading to a more accurate and robust solution for reducing metal artifacts in CT images. This approach can provide better metal artifact reduction than either approach alone or other MAR methods that rely solely on empirical or model-based approaches. Additionally, the additional processing time using ADN can be negligible because many CT slices can be

forwarded to the model, as the GPU memory capacity allows. Whether only one CT slice or multiple CT slices are being processed, it takes approximately a second or less.

Reconstructions performed with the JawEquivPhantom demonstrated that CBHE-based MAR can be applied to cases containing metallic objects of several types by separately performing MAR for each metal. Specifically, it follows a sequential process of performing MAR on the metal with the lowest density in the entire metal area and then on the metal with the next-lowest density, while excluding the previous metal area. Therefore, the proposed method can reveal artifacts not only between the same metals but also between different metals. In the proposed hybrid approach, the image quality of volumetric CBCT imaging was similar or superior to that of the sinogram inpainting-based and model-based approaches without losing morphological information locally. Quantitative analysis using MAD and CNR calculations substantiated the increased quality of the reconstructed images. Furthermore, LIMAR and NMAR showed better MAD values for the JawEquivPhantom. However, they lost the anatomical shape around the metal area. Thus, they had lower CNR values with and without ADN.

Although the proposed hybrid scheme can effectively correct metal-induced artifacts in dental CBCT images, our future work should be improved. First, as it inherits the CBHE, it has identical dependencies on accurately segmenting the metal region, X-ray spectrum information, etc. Second, the ADN-based post-refinement stage is vulnerable to mapping input data to the desired format. Even small changes in the mapping range can yield significantly different results. Third, as shown in Fig. 2, the CBHE model can provide a good approximation when the metal length is < 50 mm. If the ray transmission length of the metal is > 50 mm, more experiments are required to test the feasibility of this hybrid scheme. Fourth, our method should be explored further because of the limited data available in this study. Only one dental phantom was used as validation data. As proof of concept, we demonstrated the feasibility of using the proposed hybrid method to correct metal artifacts in dental CBCT. Fifth, the currently designed learning model has a size limitation of 256×256 as an input, which requires additional downsampling and upsampling before and after passing through the model. Modifying the model to enable inputs of 512×512 would eliminate the requirement for samplings that are no longer needed. However, this may increase GPU memory requirements slightly by a factor of two or less.

5. Conclusions

We developed a hybrid MAR approach based on CBHE-based mathematical correction followed by post-refinement with a CycleGAN-based ADN and validated its performance through phantom measurement data. The hybrid approach can be a powerful tool for improving the quality of CBCT images in the presence of metal artifacts. By combining the strengths of both approaches, this hybrid method can provide a more accurate and robust solution for reducing metal artifacts and improving the detection of areas of interest in dentomaxillofacial applications.

Submission checklist

A cover letter. It must include your name, address, telephone and fax numbers, and e-mail address, and state that all authors have contributed to the paper and have never submitted the manuscript, in whole or in part, to other journals. Conflict of interest disclosure statement (see the relevant section). Permission letter(s) from copyright holder(s), if any. If material has been reproduced from other copyrighted sources, the letter(s) of permission from the copyright holder(s) to use the copyrighted sources must be supplied.

Declaration of competing interest

The authors declare that they have no known competing financial interests or personal relationships that could have appeared to influence the work reported in this paper.

Acknowledgements

This study was presented at the International Conference on Nuclear Analytical Techniques in 2022 (NAT2022), which was held in Daejeon, Korea, from December 7 to 9, 2022. This study was supported by a faculty research grant from Yonsei University College of Medicine for 2022 (6-2022-0064) and the National Research Foundation of Korea (NRF) funded by the Korea government (MSIT) (2022R1A2C2011556).

References

[1] W.A. Kalender, R. Hebel, J. Ebersberger, Reduction of CT artifacts caused by metallic implants, Radiology 164 (2) (1987) 576–577.
[2] S. Zhao, K.T. Bae, B. Whiting, G. Wang, A wavelet method for metal artifact reduction with multiple metallic objects in the field of view, J. X Ray Sci. Technol. 10 (1) (2002) 67–76, 2.
[3] M. Bal, L. Spies, Metal artifact reduction in CT using tissue-class modeling and adaptive prefiltering, Med. Phys. 33 (8) (2006) 2852–2859.
[4] X. Duan, L. Zhang, Y. Xiao, J. Cheng, Z. Chen, Y. Xing, Metal Artifact Reduction in CT Images by Sinogram TV Inpainting, 2008 IEEE Nuclear Science Symposium Conference Record, IEEE, 2008, pp. 4175–4177.
[5] D. Prell, Y. Kyriakou, M. Beister, W.A. Kalender, A novel forward projection-based metal artifact reduction method for flat-detector computed tomography, Phys. Med. Biol. 54 (21) (2009) 6575.
[6] E. Meyer, R. Raupach, M. Lell, B. Schmidt, M. Kachelrieß, Normalized metal artifact reduction (NMAR) in computed tomography, Med. Phys. 37 (10) (2010) 5482–5493.
[7] Y. Li, X. Bao, X. Yin, Y. Chen, L. Luo, W. Chen, Metal Artifact Reduction in CT Based on Adaptive Steering Filter and Nonlocal Sinogram Inpainting, 2010 3rd International Conference on Biomedical Engineering and Informatics, IEEE, 2010, pp. 380–383.
[8] H.S. Park, J.K. Choi, K.-R. Park, K.S. Kim, S.-H. Lee, J.C. Ye, J.K. Seo, Metal artifact reduction in CT by identifying missing data hidden in metals, J. X Ray Sci. Technol. 21 (3) (2013) 357–372.
[9] A. Mehranian, M.R. Ay, A. Rahmim, H. Zaidi, X-Ray CT metal artifact reduction using wavelet domain L_0 sparse regularization, IEEE Trans. Med. Imag. 32 (9) (2013) 1707–1722.
[10] G. Wang, D.L. Snyder, J.A. O'Sullivan, M.W. Vannier, Iterative deblurring for CT metal artifact reduction, IEEE Trans. Med. Imag. 15 (5) (1996) 657–664.
[11] B. De Man, J. Nuyts, P. Dupont, G. Marchal, P. Suetens, Reduction of metal streak artifacts in x-ray computed tomography using a transmission maximum a posteriori algorithm, IEEE Trans. Nucl. Sci. 47 (3) (2000) 977–981.
[12] B. De Man, J. Nuyts, P. Dupont, G. Marchal, P. Suetens, An iterative maximum-likelihood polychromatic algorithm for CT, IEEE Trans. Med. Imag. 20 (10) (2001) 999–1008.
[13] I.A. Elbakri, J.A. Fessler, Segmentation-free statistical image reconstruction for polyenergetic X-ray computed tomography, in: Proceedings IEEE International Symposium on Biomedical Imaging, IEEE, 2002, pp. 828–831.
[14] C. Lemmens, D. Faul, J. Nuyts, Suppression of metal artifacts in CT using a reconstruction procedure that combines MAP and projection completion, IEEE Trans. Med. Imag. 28 (2) (2009) 250–260.
[15] J. Wang, L. Xing, A binary image reconstruction technique for accurate determination of the shape and location of metal objects in x-ray computed tomography, J. X Ray Sci. Technol. 18 (4) (2010) 403–414.
[16] J. Hsieh, R.C. Molthen, C.A. Dawson, R.H. Johnson, An iterative approach to the beam hardening correction in cone beam CT, Med. Phys. 27 (1) (2000) 23–29.
[17] H.S. Park, D. Hwang, J.K. Seo, Metal artifact reduction for polychromatic X-ray CT based on a beam-hardening corrector, IEEE Trans. Med. Imag. 35 (2) (2016) 480–487.
[18] H. Shi, Z. Yang, S. Luo, Reduce beam hardening artifacts of polychromatic X-ray computed tomography by an iterative approximation approach, J. X Ray Sci. Technol. 25 (3) (2017) 417–428.
[19] J. Hur, D. Kim, Y.-G. Shin, H. Lee, Metal artifact reduction method based on a constrained beam-hardening estimator for polychromatic x-ray CT, Phys. Med. Biol. 66 (6) (2021), 065025.
[20] H.S. Park, S.M. Lee, H.P. Kim, J.K. Seo, Y.E. Chung, CT sinogram-consistency learning for metal-induced beam hardening correction, Med. Phys. 45 (12) (2018) 5376–5384.

[21] L. Gjesteby, Q. Yang, Y. Xi, Y. Zhou, J. Zhang, G. Wang, Deep learning methods to guide CT image reconstruction and reduce metal artifacts, in: Medical Imaging 2017: Physics of Medical Imaging, International Society for Optics and Photonics, 2017, 101322W.
[22] I. Goodfellow, J. Pouget-Abadie, M. Mirza, B. Xu, D. Warde-Farley, S. Ozair, A. Courville, Y. Bengio, Generative Adversarial Nets, Adv. Neural Inf. Process. Syst., 2014, pp. 2672–2680.
[23] P. Isola, J.-Y. Zhu, T. Zhou, A.A. Efros, Image-to-image translation with conditional adversarial networks, in: Proceedings of the IEEE Conference on Computer Vision and Pattern Recognition, 2017, pp. 1125–1134.
[24] M.U. Ghani, W.C. Karl, Fast enhanced CT metal artifact reduction using data domain deep learning, IEEE Trans. Comput. Imaging 6 (2019) 181–193.
[25] H. Zhao, O. Gallo, I. Frosio, J. Kautz, Loss functions for image restoration with neural networks, IEEE Trans. Comput. Imaging 3 (1) (2016) 47–57.
[26] H. Liao, W.-A. Lin, S.K. Zhou, J. Luo, ADN: artifact disentanglement network for unsupervised metal artifact reduction, IEEE Trans. Med. Imag. 39 (3) (2020) 634–643.
[27] W.-A. Lin, H. Liao, C. Peng, X. Sun, J. Zhang, J. Luo, R. Chellappa, S.K. Zhou, Dudonet: dual domain network for ct metal artifact reduction, Proceedings of the IEEE/CVF Conference on Computer Vision and Pattern Recognition (2019) 10512–10521.
[28] B. Zhou, X. Chen, S.K. Zhou, J.S. Duncan, C. Liu, DuDoDR-Net: dual-domain data consistent recurrent network for simultaneous sparse view and metal artifact reduction in computed tomography, Med. Image Anal. 75 (2022), 102289.
[29] H. Wang, Y. Li, H. Zhang, D. Meng, Y. Zheng, InDuDoNet+: a deep unfolding dual domain network for metal artifact reduction in CT images, Med. Image Anal. 85 (2023), 102729.
[30] L.A. Feldkamp, L. Davis, J.W. Kress, Practical cone-beam algorithm, J. Opt. Soc. Am. A 1 (6) (1984) 612–619.
[31] J. Hubbell, S. Seltzer, X-ray mass attenuation coefficients. https://www.nist.gov/pml/x-ray-mass-attenuation-coefficients, 2004.
[32] M. Nakao, K. Imanishi, N. Ueda, Y. Imai, T. Kirita, T. Matsuda, Regularized three-dimensional generative adversarial nets for unsupervised metal artifact reduction in head and neck CT images, IEEE Access 8 (2020) 109453–109465.
[33] K. Yan, X. Wang, L. Lu, R.M. Summers, DeepLesion: automated mining of large-scale lesion annotations and universal lesion detection with deep learning, J. Med. Imag. 5 (3) (2018), 036501-036501.
[34] B. Glocker, D. Zikic, E. Konukoglu, D.R. Haynor, A. Criminisi, Vertebrae localization in pathological spine CT via dense classification from sparse annotations, in: Medical Image Computing and Computer-Assisted Intervention–MICCAI 2013: 16th International Conference, Nagoya, Japan, 2013, pp. 262–270. September 22-26, 2013, Proceedings, Part II 16, Springer.
[35] H. Lee, B.P. Fahimian, L. Xing, Binary moving-blocker-based scatter correction in cone-beam computed tomography with width-truncated projections: proof of concept, Phys. Med. Biol. 62 (6) (2017) 2176.